

Imaging subcellular dynamics with fast and light-efficient volumetrically parallelized microscopy: supplementary material

KEVIN M. DEAN,^{1,2} PHILIPPE ROUDOT,^{1,2} ERIK S. WELF,^{1,2} THERESA POHLKAMP³,
GERARD GARRELTS⁴, JOACHIM HERZ³, RETO FIOKA^{1,*}

¹Department of Cell Biology. UT Southwestern Medical Center, 6000 Harry Hines Blvd., Dallas, Texas, USA

²Lyda Hill Department of Bioinformatics. UT Southwestern Medical Center, 6000 Harry Hines Blvd., Dallas, Texas, USA

³Department of Molecular Genetics. UT Southwestern Medical Center, 6000 Harry Hines Blvd., Dallas, Texas, USA

⁴Coleman Technologies. 5131 West Chester Pike, Newtown Square, Pennsylvania, USA

*Corresponding author: Reto.Fiolka@UTsouthwestern.edu

Published 17 February 2017

This document contains the supplementary information for the manuscript “Imaging subcellular dynamics with fast and light-efficient volumetrically parallelized microscopy,” <https://doi.org/10.1364/optica.4.000263>. It provides video captions, two supplementary notes, two supplementary tables, eight supplementary figures, and supplementary references. © 2017 Optical Society of America

<https://doi.org/10.1364/optica.4.000263.s001>

1. Supplementary Visualization Captions

Visualization 1. Migrating MDA-MB-231 breast cancer cell, labeled with EGFP-Tractin. Camera integration time, 10 ms. Stack acquisition time, 1.36 seconds. Total Z-stacks, 1500.

Visualization 2. Vimentin dynamics at the leading of a wound response by a population of RPE cells. XY maximum intensity projection. Cells are genome modified to express mEmerald-tagged vimentin from a single allele. Camera integration time, 10 ms. Stack acquisition time, 5.69 seconds. High frequency ringing on some bright fibers is likely a deconvolution artifact. Total Z-stacks, 1000. Scale bar 10 microns.

Visualization 3. Filopodial dynamics in an RPE cell, labeled with mNeonGreen-Lifeact-7. XY maximum intensity projection with stack registration, gamma 0.85. Camera integration time, 20 ms. Stack acquisition time, 1.36 seconds. Total Z-stacks, 180. Scale bar 10 microns.

Visualization 4. Microtubule plus tips in a confluent layer of U2OS cells, labeled with mNeonGreen-EB3-7. Camera integration time, 25 ms. Stack acquisition time, 1.70 seconds. Total Z-stacks, 50. Photobleaching correction applied (ImageJ plugin, method: histogram matching).

Visualization 5. Early endosome transport in a Cho-K1 cell, labeled with mNeonGreen-Rab5a-7. XY maximum intensity projection. Camera integration time, 5 ms. Stack acquisition time, 342 ms. Total Z-stacks, 500. Scale bar 10 microns.

Visualization 6. Early endosome transport in a RPE cell, labeled with mNeonGreen-Rab5a-7. Camera integration time, 2 ms. Stack acquisition time, 138 ms. Total Z-stacks, 400. Scale bar 10 microns.

Visualization 7. Calcium signaling in primary cortical neurons, labeled with GCaMP-6f. Colored regions represent action potentials, identified through a temporal FFT. Camera integration time, 1 ms. Stack acquisition time, 69.6 ms. Total Z-stacks, 400.

2. Supplementary Notes

Supplementary Note 1. Comparison to other 3D Parallelized Fluorescence Microscopes

In this note we compare the light losses and out-of-focus contamination of other parallelized 3D acquisition schemes, including both refractive [1] and diffractive [2, 3] methods. With these methods, when N focal planes are imaged simultaneously, the in-focus signal from every focal plane is reduced N-fold, and every plane receives out-of-focus light from N-1 other planes. Thus, 3-fold parallelization is

accompanied with a 66% decrease in fluorescence intensity. This is worsened for binary diffractive systems, which introduce an additional loss of light due to limited diffraction efficiencies.

This limitation is not present in pLSFM, which offers lossless imaging over a finite depth, except for minor reflective losses on the order of a few percent introduced by mirrors and relay lenses. This lossless region extends $\sim 13 \mu\text{m}$ in the laser propagation (Y) direction (see Note S2). While imaging within this region, pLSFM does not suffer from cross-talk between image planes. Imaging outside of this region is still possible, but the detection efficiency linearly decreases with distance from the coverslip (Figure S4 and S5). This results from clipping of the light by the preceding knife-edge mirror. Compared to previous parallelized acquisition schemes, at $N=3$, pLSFM remains more efficient over fields of view extending more than $20 \mu\text{m}$ in the Y-direction.

For the special case of $N=2$, there is a different class of microscopes that can observe the sample from two opposing directions. [4]. Such microscopes overcome light losses associated with parallelization by effectively doubling their detection NA, but do not overcome cross-talk. Furthermore, these methods cannot be extended to higher degrees of parallelization in a straightforward manner.

Supplementary Note 2. Illumination and Detection of Multiple, staggered image planes

Both the injection of the three light-sheets, as well as the pick-up of the corresponding three image planes, is performed in image space of the illumination and detection path, respectively. While both are physically realized the same way, by reflection from staggered knife edge mirrors, the pick-up of the three images is more demanding: first, an entire image needs to be reflected without affecting the adjacent images, whereas in the illumination path, only a narrow line needs to be reflected. Second, for diffraction limited imaging, the full NA of the detection objective needs to be used, whereas the illumination only requires a subset of the available NA for the creation of the light-sheets.

Our microscope design allows in theory lossless (in the sense that no further light losses are introduced compared to single plane detection) imaging of multiple planes over a finite field of view. To understand the interplay of the different design parameters we analyze the system with ray optics in image space and perform experiments to validate the theoretical predictions. In Fig. S4A, the position of the light-sheets (shown as green bars) in sample space are shown. A necessary condition for lossless detection is that the inclination angle β of the coverslip must be larger than the half angle α of the detection objective.

Figure S4B shows the basic image formation of two light-sheets. In light-sheet I, the point closest to the coverslip is imaged on the edge of the mirror 1. A lossless image of light-sheet II can be formed as long as no fluorescence is incorrectly picked-off by mirror 1. This condition can be estimated with ray tracing in image space as the angles are relatively small.

The lateral separation d' of the two light-sheets in image space is given by:

$$d' = L \cdot \sin(\beta) \cdot M \quad (\text{S1})$$

With a refractive index of the immersion media of η , a magnification of the detection arm of M , pupil radius of r_p , tube lens focal length f_{tub} , the half angle (α'), axial (h') and lateral (x') separation of the light-sheets in image space are given by:

$$h' = L \cdot \cos(\beta) \cdot M^2 / \eta \quad (\text{S2})$$

$$y' = d' - h' \cdot \tan(\alpha') \quad (\text{S3})$$

$$\alpha' = \tan^{-1}(r_p / f_{\text{tub}}) \quad (\text{S4})$$

With the values listed in Table S2, we find that for light sheet II the maximum range before any clipping occurs is $y = y' / M = 13 \mu\text{m}$.

In practice, the placement of the sample is important to realize the best imaging performance. Figure S4C illustrates the ideal scenario, where features close to the coverslip are imaged right on the edge of the pick-up mirrors. Figs. S4D-E show two scenarios where the sample image is misplaced in the Y-direction.

To empirically estimate the distance y over which an image can be formed without loss of light due to cross-talk, we performed the following experiment: a coverslip with surface immobilized 200 nm fluorescent beads was oriented parallel to the XY plane and was focused sequentially on each camera (Fig. S5A). Fluorescence was generated with an appropriately bandpass filtered metal halide lamp aligned to provide Kohler-like illumination from the excitation objective. The beads on the coverslip were scanned in 160 nm steps in the Y-direction across the field of view of the corresponding detection camera. A maximum intensity projection in the scan dimension of the resulting image stack was taken to yield tracks of the beads. To ensure that most tracks were complete (i.e. the bead contributing to the track was scanned over the entire field of view), small islands of beads were located on the coverslip and the scan range was adjusted that the islands were scanned beyond the field of view in both directions. The intensity of the bead tracks was averaged in the X-direction over $\sim 3 \text{ microns}$ in an area free of dust and other contamination to yield an intensity decay curve in the Y-direction.

The evenness of the illumination was first tested on Camera 1, because it has no hard limit on its field of view. Since there is no preceding mirror, we assume that the detection itself should be even within the limitations of the objective design for this image plane. The fluorescence rises sharply at the mirror edge (Fig S5C and D) and remains constant within $\sim 5\%$ for over 40 microns . While the evenness of the illumination was not perfect, it appeared sufficient for a range of a few tens of microns.

For image plane 2, the intensity first rises sharply and remains high as long as no light is clipped by the mirror for the preceding image plane (Mirror 1, see also Figure S5B). As soon as clipping occurs, the intensity gradually decreases (Fig. S5C and D).

Image Plane 3 is transmitted and has no mirror edge within its field of view. Therefore, the intensity profile is expected to remain uniform until beam clipping by the preceding mirror 2 occurs, which is supported by our measurement (Fig. S5C and D).

To align the intensity curve of image plane 3 to the other two curves, we used a conventional pLSFM stacks with beads immobilized on a coverslip. The sample was placed as close as possible to the edges of the pick off mirrors for image plane 1 and 2. The resulting Y-position of the beads in Image plane 1 defined the start of the effectively useful range of the field of view on camera 3. To put it differently, while image plane 3 has no restriction of its field of view in the negative Y-direction, this additional area cannot be used in practice - excessive image clipping would result in the other two image planes (see also Figure S4D).

The effectively usable field of view is indicated by a dashed line in Figs. S5C and D. It is to the left limited by the mirror edge step response of image plane 1 and 2 and to the right by the onset of beam clipping on image plane 2 and 3. We estimated that within 13 microns, the intensity remained within 95% of the peak intensity. Of note, the mirror edge step response for image plane 2 is wider than for image plane 1, most likely to a less perfect mirror edge. If image plane 2 had a similar edge response as image plane 3, the effective field of view would become almost a micron wider. Thus, we assume that our image formation theory slightly underestimates the effective field of view.

Reasons for deviations from the theory could be: the objective may not be performing at its nominal NA, the mirror might not be perfectly conjugate to the sample plane, the knife-edge mirrors may not be perfectly sharp, and the tube lens may not be perfectly telecentric. The latter point is evidenced that the magnification slightly grows with increasing distance from the tube lens (40, 40.2, 40.5 for the three views used in this manuscript). Thus, the image forming rays slightly diverge in image space.

3. Supplementary Tables

	Camera 1 raw / deconvolved (nm)	Camera 2 raw / deconvolved (nm)	Camera 3 raw / deconvolved (nm)
Lateral Resolution x	467 ± 6 / 345 ± 21	435 ± 7 / 315 ± 10	489 ± 15 / 353 ± 16
Lateral Resolution y	381 ± 6 / 275 ± 11	407 ± 14 / 287 ± 16	463 ± 9 / 325 ± 10
Axial Resolution	908 ± 24 / 631 ± 24	950 ± 18 / 640 ± 27	919 ± 21 / 618 ± 16

Supplementary Table 1. Measured resolution for pLSFM. Mean and standard deviation (N=10) of resolution, reported at full width half maximum, of 100 nm fluorescent nanospheres. Due to an imperfect objective/tube lens combination, a lateral astigmatism results in minor differences in the X and Y resolutions.

Variable name	Value	description
L	36 μ m	Separation of light-sheets
α	37 deg	Opening angle of NA=0.8 water objective
β	49 deg	Inclination of cover slip
M	40.2	Averaged Magnification of detection arm
F_tub	200 mm	Focal length of tube lens
rp	4 mm	Pupil radius

Supplementary Table 2. Design parameters of pLSFM microscope.

4. Supplementary Figures

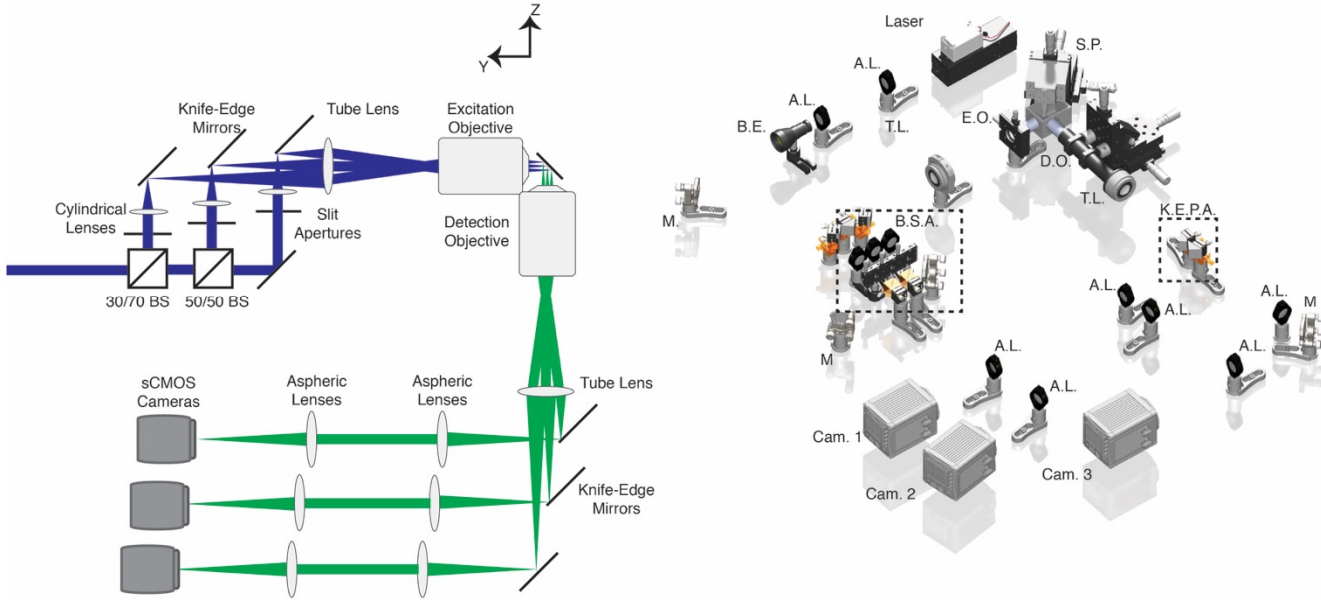


Figure S1. (Left) Optical geometry of the pLSFM microscope. A digitally modulated laser is spatially filtered with a pinhole and expanded with a telescopic beam expander (not shown), directed through a series of beam splitters, slit apertures, and cylindrical lenses. The slit apertures are conjugate to the front-pupil plane of the cylindrical lenses and the back-pupil plane of the excitation objective, and are used to adjust the excitation numerical aperture of the illumination beam in the sample plane. Knife-edge mirrors pick-off the focused illumination beams, directing them to a tube lens and excitation objective. Only the middle beam is fully collimated by the tube lens, and defocus is used to displace the first and third beams in the Y-direction. Fluorescence is collected at 90 degrees with the detection objective, and the fluorescence from each illumination beam is imaged onto a series of knife-edge mirrors, before being relayed to 3 scientific complementary metal oxide semiconductor cameras (sCMOS) with a 1:1 telescope consisting of two aspheric lenses. (Right) A computer-aided design rendering of the light-sheet microscope. 488 nm solid state laser (Laser). Achromatic doublet lens (A.L.). Telescopic beam expander (B.E.). Mirror (M.) Beam splitter array (B.S.A., see Figure S2). Tube Lens (T.L.). Excitation Objective (E.O.). Detection Objective (D.O.). Sample Piezo (S.P.). Knife-Edge Prism Assembly (K.E.P.A.). sCMOS Cameras (Cam. 1, Cam. 2, and Cam. 3).

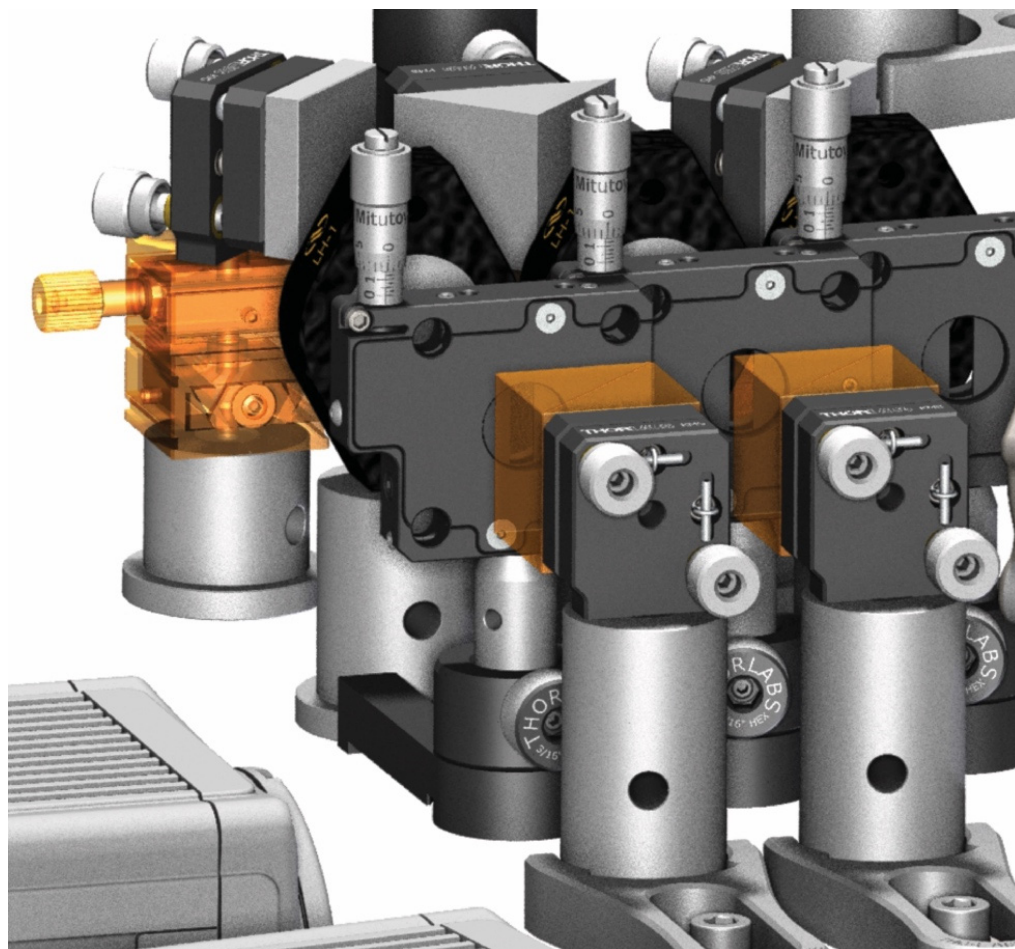


Figure S2. Beam Splitter Assembly. Collinearly aligned laser light is directed through two consecutive beam splitters with 30/70 and 50/50 percent reflection/transmission, respectively, generating three approximately equal intensity laser beams. Each beam is truncated by a variable slit width aperture located in the Fourier plane of a cylindrical lens, which focuses the laser light to a 1D Gaussian line on a series of knife-edge mirrors, which are imaged with a tube lens and excitation objective to the sample plane.

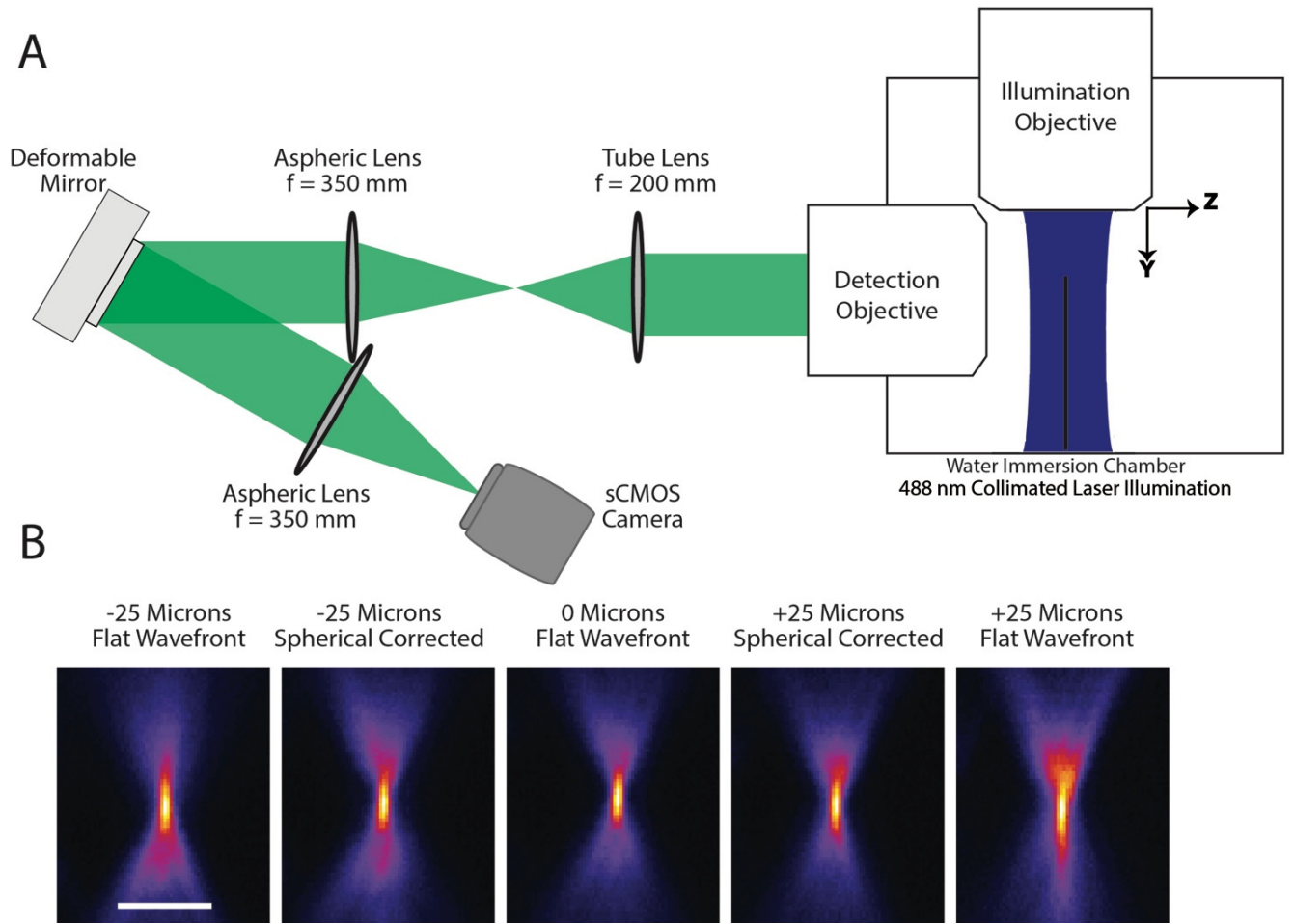


Figure S3. Removal of spherical aberration with a deformable mirror. (A) Schematic drawing of imaging system used for correcting spherical aberrations. Beads on a coverslip (black line) were kept stationary at the center of a collimated 488 nm laser (blue) for illumination. The detection objective was equipped with a piezo actuator to allow z-stepping. The pupil plane of the detection objective was imaged onto a deformable mirror. The objective and sCMOS camera could be translated along the optical axis to re-focus outside of the nominal focal plane. (B) Axial cross-sections of single 200 nm beads at the nominal focal plane, and 25 microns above and below the nominal focal plane with and without compensation of spherical aberrations. A positive sign means here a movement of the objective in the positive direction of the z-axis. For -25 microns (corresponding to image plane 1), compensation of spherical aberrations improved the bead intensity from 75% to 90% compared to the imaging at the nominal focal plane. For +25 microns (corresponding to image plane 3) compensation of spherical aberrations improved the bead intensity from 78% to 98% compared to the imaging at the nominal focal plane.

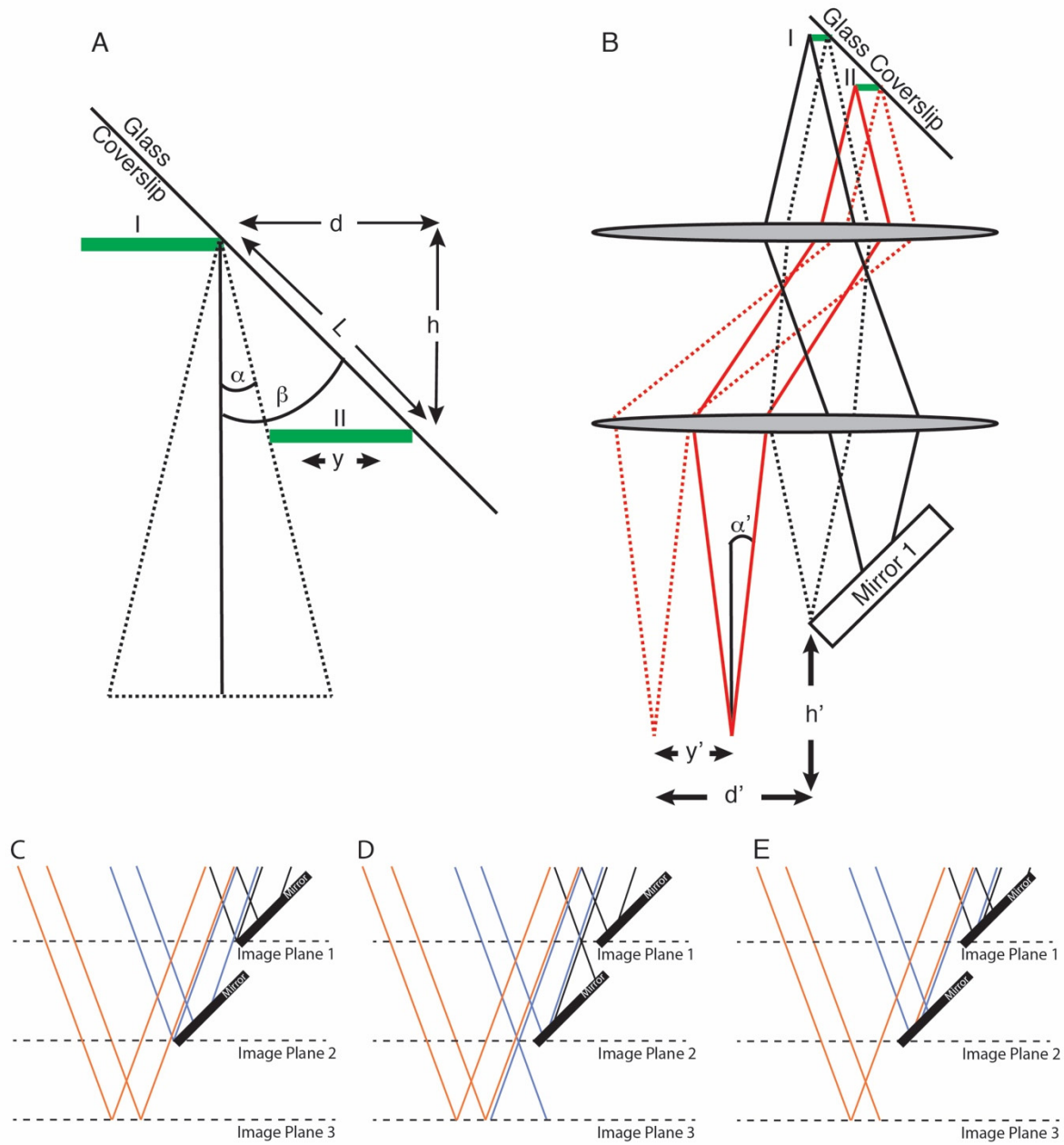


Figure S4. Sample height, geometric constraints, and image crosstalk. (A) Location of light-sheets, inclination angle of coverslip and detection cone. Diffraction effects are ignored for simplicity. (B) Image formation of two staggered light-sheets using ray optics. (C) Ideal alignment: fluorescence emission from objects on the coverslip is imaged on the edges of the pick off mirrors. For image plane 2 and 3, fluorescence light will be collected without crosstalk over the largest possible distance y . (D) Suboptimal scenario I: the sample is placed too far to the left and fluorescence light corresponding to regions close to the coverslip miss the edges of the pick off mirrors. Features close to the coverslip will be missed on camera 1 and 2. (E) Suboptimal scenario II: the image of the sample is placed too far to the right. The field of view over which cross-talk free imaging occurs becomes smaller for image plane 2 and image plane 3, as beam clipping by preceding mirrors occurs earlier.

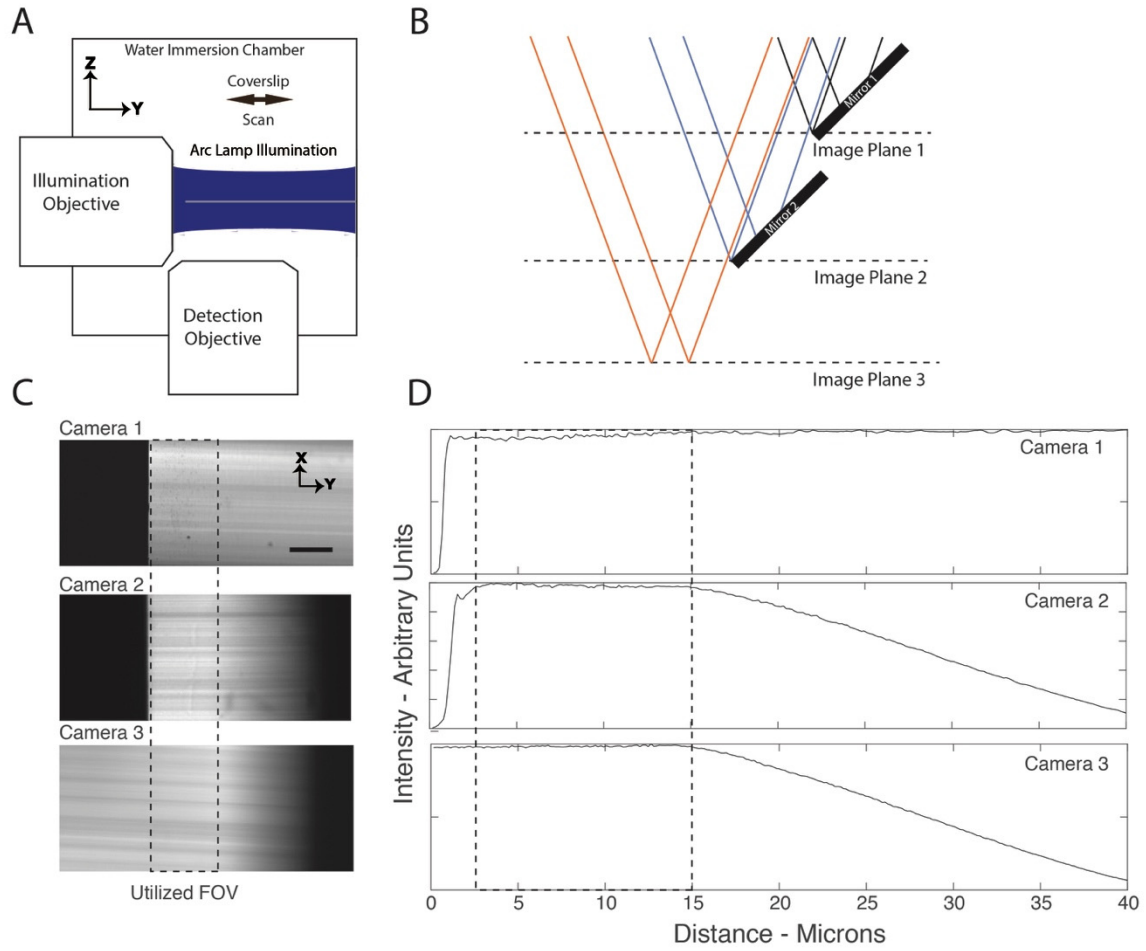


Figure S5. Measurement of the effective field of view. (A) To determine the size of the field of view in the Y-direction that can effectively be picked off by the knife-edge mirrors without losses in collection efficiency, we scanned surface immobilized beads on a coverslip (gray line) in the Y-direction, in the focal plane for each camera. The sample was illuminated via the illumination objective with an incoherent light (blue). (B). Sketch of the pick off mirrors. Cameras 1 and 2 lose fluorescence abruptly when the light rays miss the edge of the knife-edge mirror. Camera 2 and 3 will gradually lose light when light clipping from preceding mirrors occurs. (C) Images were acquired of beads as they were scanned in the Y-direction, and the maximum value for each pixel position is shown here. (D) Normalized fluorescence intensity as a function of Y-position in the image field of view. The extent in the Y-direction over which cross-talk free widefield imaging results is indicated with dashed lines. Scale bar 10 μm .

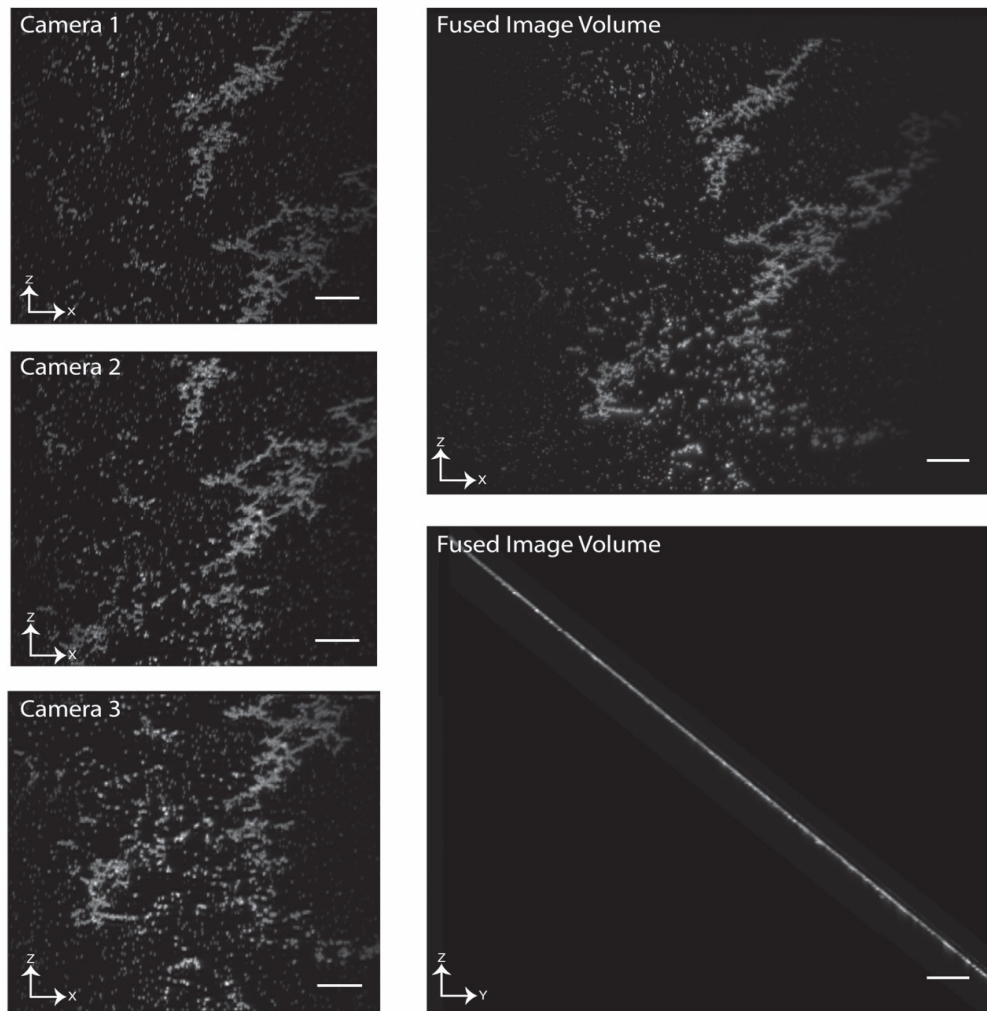


Figure S6. Bead dataset for image fusion calibration. (Left) Images of dense coverslip-bound 200 nm fluorescent beads are acquired on the three cameras for the full 100 μm of the piezo scan range. Data shown as maximum intensity projections. (Right) The relative positioning of the three cameras in image space is estimated using a fully automated multipyramidal image registration algorithm. Maximum intensity projections in lateral and axial dimensions shown for deconvolved, affine transformed, and sheared data. Scale bars 10 μm .

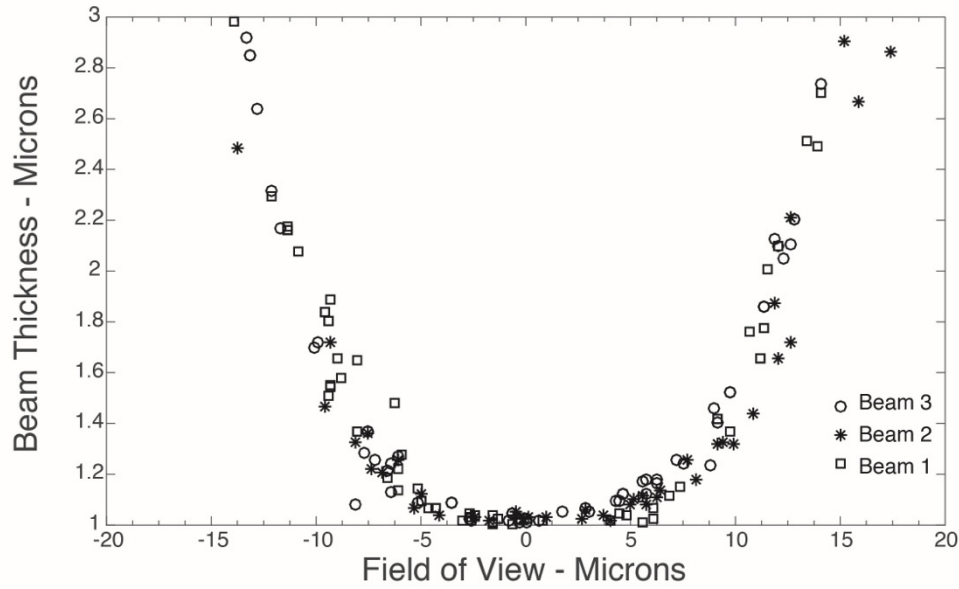
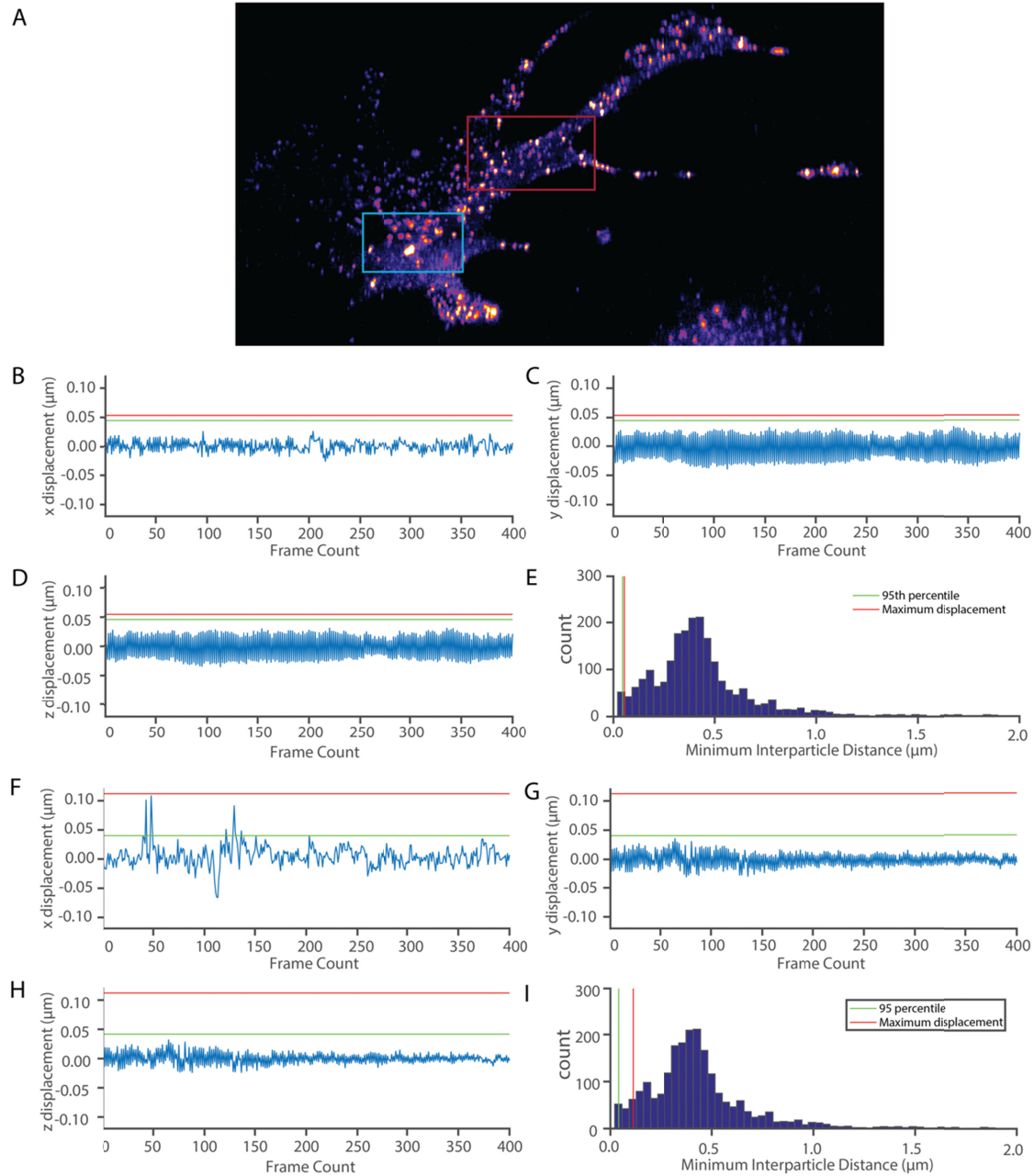


Figure S7. Experimentally measured thickness of the three light sheets. Local beam thickness was measured by scanning fluorescent sub-diffraction beads through each illumination beam, and measuring the axial intensity distribution at full width half maximum for individual beads at different beam positions. To exclude the influence of the detection OTF, the bead intensity was integrated over a lateral region of interest that contained the entire PSF. Raw data of three measurement runs for the three beams are shown. The mean and standard deviation are $1.03 \pm 0.02 \mu\text{m}$, $1.02 \pm 0.01 \mu\text{m}$, and $0.98 \pm 0.01 \mu\text{m}$, for beams 1, 2, and 3, respectively. The Rayleigh ranges were found with cubic interpolation of the measured values $7.6 \pm 0.2 \mu\text{m}$, $8.2 \pm 0.2 \mu\text{m}$, and $7.4 \pm 0.2 \mu\text{m}$, for beams 1, 2, and 3, respectively.



5.

Figure S8. Oscillations introduced by rapid sample scanning. (A) Sub-regions used for analysis of the 7.26 Hz Rab5a dataset. Oscillations measured by looking at the frame-to-frame displacement of detected particles in a region with (blue) and without (red) stitching overlap between sub-volumes. (B-D) Region with stitching overlap. Plots provide the average frame-to-frame displacement for each independent axis. Because sample scanning occurs intermediate to the Y and Z axes, the amplitude of vibrations in these axes are significantly larger than the non-scanned, X-axes. In each case, the maximum displacement was ~25 nm. (E) Histogram of inter-particle distance, with the 95th percentile and maximum vibration amplitude indicated. (F-I). Similar analysis of vibrations in a region without stitching overlap. In both cases, the minimum inter-particle distance is ~450 nm, which is significantly larger than the uncertainty introduced by image oscillations. Thus, the vibrations do not appear to introduce ambiguity in the particle tracking results.

5. Supplementary References

1. S. Geissbuehler, A. Sharipov, A. Godinat, N. L. Bocchio, P. A. Sandoz, A. Huss, N. A. Jensen, S. Jakobs, J. Enderlein, F. Gisou van der Goot, E. A. Dubikovskaya, T. Lasser, and M. Leutenegger, "Live-cell multiplane three-dimensional super-resolution optical fluctuation imaging," *Nature Communications* **5**, 5830 (2014).
2. S. Abrahamsson, J. Chen, B. Hajj, S. Stallinga, A. Y. Katsov, J. Wisniewski, G. Mizuguchi, P. Soule, F. Mueller, C. D. Darzacq, X. Darzacq, C. Wu, C. I. Bargmann, D. A. Agard, M. Dahan, and M. G. L. Gustafsson, "Fast multicolor 3D imaging using aberration-corrected multifocus microscopy," *Nature Methods* **10**, 60-63 (2012).
3. S. Abrahamsson, R. Ilic, J. Wisniewski, B. Mehl, L. Yu, L. Chen, M. Davanco, L. Oudjedi, J.-B. Fiche, B. Hajj, X. Jin, J. Pulupa, C. Cho, M. Mir, M. El Beheiry, X. Darzacq, M. Nollmann, M. Dahan, C. Wu, T. Lionnet, J. A. Liddle, and C. I. Bargmann, "Multifocus microscopy with precise color multi-phase diffractive optics applied in functional neuronal imaging," *Biomedical Optics Express* **7**, 855 (2016).
4. R. K. Chhetri, F. Amat, Y. Wan, B. Höckendorf, W. C. Lemon, and P. J. Keller, "Whole-animal functional and developmental imaging with isotropic spatial resolution," *Nature Methods* **12**, 1171-1178 (2015).